The Astrophysical Journal, 608:179–188, 2004 June 10

XMM-NEWTON OBSERVATION OF THE MERGING GALAXY CLUSTER A1644

Thomas H. Reiprich and Craig L. Sarazin
Department of Astronomy, University of Virginia, P.O. Box 3818, Charlottesville, VA 22903-0818; thomas@reiprich.net, sarazin@virginia.edu

Joshua C. Kempner
Harvard-Smithsonian Center for Astrophysics, 60 Garden Street, MS-67, Cambridge, MA 02138; jkempner@cfa.harvard.edu

and

Eric Tittley
Institute for Astronomy, University of Edinburgh, Edinburgh, EH9 3HJ, UK; ert@roe.ac.uk
Received 2003 August 14; accepted 2004 February 19

ABSTRACT

We present an *XMM-Newton* imaging spectroscopy analysis of the galaxy cluster A1644. A1644 is a complex merging system consisting of a main cluster and a subcluster. A trail of cool, metal-rich gas has been discovered close to the subcluster. The combination of results from X-ray, optical, and radio data and a comparison to a hydrodynamic simulation suggest that the subcluster has passed by the main cluster off-axis and that a fraction of its gas has been stripped off during this process. Furthermore, for this merging system simple effects are illustrated that can affect the use of clusters as cosmological probes. Specifically, double clusters may affect estimates of the cluster number density when treated as a single system. Mergers, as well as cool cores, can alter the X-ray luminosity and temperature measured for clusters, causing these values to differ from those expected in equilibrium.

Subject headings: cooling flows — cosmology: observations — galaxies: clusters: general — galaxies: clusters: individual (A1644) — intergalactic medium — X-rays: galaxies: clusters

1. INTRODUCTION

Clusters of galaxies are formed in violent events, cluster mergers. These mergers can dramatically affect the observed properties of clusters, particularly in the X-ray band (e.g., Markevitch et al. 2002). Signatures of mergers include "cold fronts" (Markevitch et al. 2000; Vikhlinin et al. 2001b), merger shocks (e.g., Markevitch et al. 2002), and multiple cool cores (Markevitch et al. 1999). The application of simple hydrodynamic analysis to these merger signatures allows the merger Mach number and other aspects of the merger kinematics to be determined (Vikhlinin et al. 2001b; Kempner et al. 2002; Sarazin 2002). In general, merger Mach numbers are modest, $\mathcal{M} \sim 2$.

Mergers also provide interesting tests of the role of various physics processes in clusters. For example, very strong limits have been placed on the rate of thermal conduction and diffusion (Ettori & Fabian 2000; Vikhlinin et al. 2001a; Markevitch et al. 2003) and Kelvin-Helmholtz instabilities and viscosity (Vikhlinin et al. 2001a). Mergers also provide limits on the relative roles of thermal versus nonthermal pressure sources in the intracluster medium (ICM; Markevitch et al. 1999). The role of merger shocks in accelerating relativistic particles can also be studied (Markevitch & Vikhlinin 2001). Recently, the relative distributions of gas, galaxies, and dark matter in merging clusters have been used to limit the self-collisional cross section of the dark matter (Markevitch et al. 2004); collisional dark matter has been suggested as an explanation of the mass profiles in dwarf galaxies and as a resolution of other problems (e.g., Spergel & Steinhardt 2000).

On the other hand, merger effects can complicate the use of clusters of galaxies as cosmological probes. Clusters provide a number of important cosmological tests, mainly because they are the only objects that are large enough to represent a fair sample of materials in the universe yet small enough to be relaxed (e.g., Bahcall 2000). Most analyses of clusters for cosmology assume that they are equilibrium systems; for example, the masses of clusters are often determined from hydrostatic equilibrium, or more simply by assuming an equilibrium relation between the cluster X-ray temperature or luminosity and the cluster mass. During major mergers, clusters are not in hydrostatic equilibrium. Also, compression and heating during a merger can produce a large transient increase in the X-ray temperature and luminosity (Ricker & Sarazin 2001). If equilibrium relations are applied to merging clusters, their masses can be greatly overestimated (Randall et al. 2002). This can be particularly important for high-redshift clusters; in flux-limited samples, merging clusters can be overrepresented because of their boosted X-ray luminosities. It is important to understand these effects by studying relatively nearby clusters, where more detailed dynamical information can be determined.

In this paper, we present new *XMM-Newton* observations of the A1644 cluster. Our analysis of the *Einstein* observation suggested that this cluster was undergoing a major merger. Jones & Forman (1999) classified A1644 as a double cluster with roughly equal components based on the *Einstein* image. From a deprojection analysis of the *Einstein* data, White et al. (1997) found that A1644 harbors a small cooling flow of ~12 $M_\odot$ yr^{-1}. Girardi et al. (1997) noted the possible presence of two components in the galaxy velocity distribution in the cluster and listed two subclusters as part of this cluster. They also found that the cD galaxy had a large peculiar velocity, which suggests the possible presence of minor substructure. However, in the end they classified A1644 as a regular cluster. No evidence for substructure has been found in recent optical and near-infrared observations by Tustin et al. (2001). A1644 is located close to a region of high galaxy-cluster density. It is

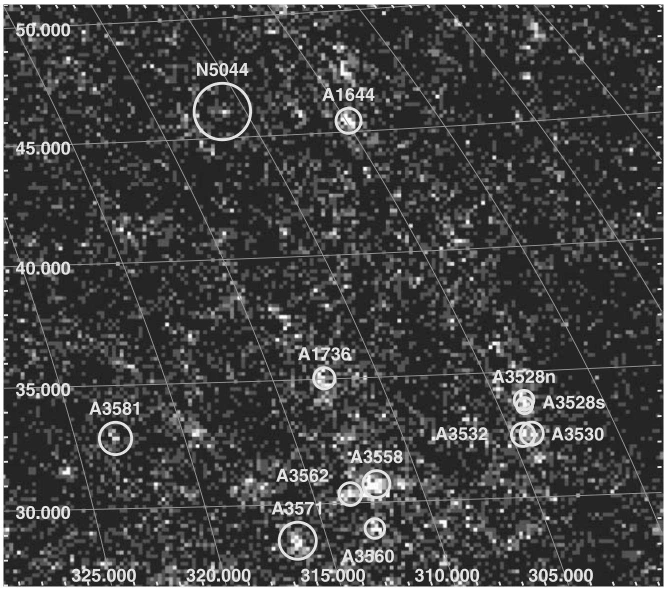

Fig. 1.—Location of A1644 relative to the core of the Shapley supercluster in Galactic coordinates. Shown are virial radii of a few clusters from Reiprich & Böhringer (2002) on top of a distribution of 2MASS galaxies.

~15° north (in Galactic coordinates) of the core of the Shapley supercluster (Fig. 1) at about the same redshift, $z(\mathrm{A1644}) = 0.0474$ (Zabludoff et al. 1993).

2. DATA REDUCTION AND ANALYSIS

XMM-Newton, with its combination of high throughput, broad spectral band, good spectral resolution, and fairly large field of view is ideal for studying this merging system. A1644 was observed by *XMM-Newton* for a total duration of 23 ks during revolution 199 (observation ID: 0010420201) on 2001 January 8. The EPIC-MOS cameras were operated in full-frame (FF) mode and the EPIC-pn camera in extended full-frame (EFF) mode. The "Thin1" filter was used in all EPIC observations for protection against optical light contamination. Calibrated event files have been created with SAS version 5.3.[1] The calibration index file was created on 2002 May 7, based on the most up-to-date calibration files available at that time. Most further reduction and analysis steps were performed using SAS version 5.3 and the software package HEAsoft, version 5.2.[2]

2.1. *Flare Rejection*

XMM-Newton observations in general suffer from periods of very high background similar to *Chandra* observations (e.g., Lumb et al. 2002). There are several possible ways to "clean" a data set of these flares. Our method is based on the fact that we will use independent blank-sky observations (§ 2.3) to determine the main nonflare hard background component, the particle-induced background (PIB). (The PIB is distinct from the flares, which are believed to be produced by "soft" protons.) Thus, we must be able to clean the blank-sky background observations in the same way as the source observation. When determining the light curve, this requires ensuring a negligible contamination by emission from astrophysical sources because otherwise the sensitivity to flare detection varies between source and background observation. Here we choose the energy band 10–12 keV for the MOS cameras and the band 12–14 keV for the pn camera, similar to previous works (e.g., Majerowicz et al. 2002), which are dominated by PIB (background induced directly or through fluorescent instrumental lines by high-energy particles) and soft protons (if present). Note that this approach has the drawback of low statistics and furthermore assumes that the flare characteristics in this energy band are representative of those at lower energies as well. In § 2.3, we test the effect of increased statistics and the latter assumption.

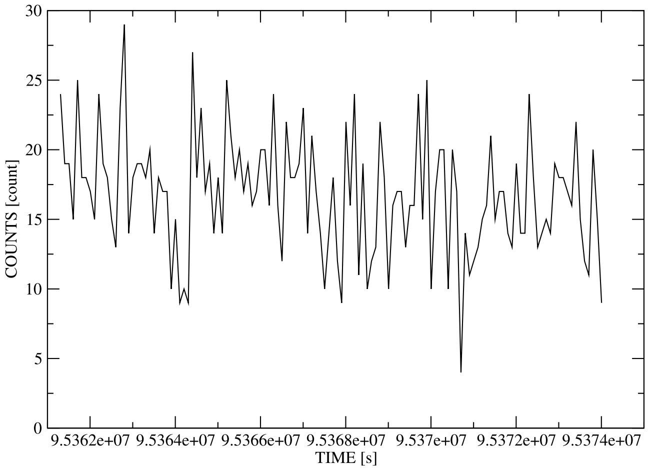

Fig. 2.—Light curve for pn with 100 s binning.

Times were binned in 100 s intervals, which appears to be a reasonable compromise between good temporal resolution and low noise level. This time interval also is large compared to the readout cycles of the cameras. Furthermore, only events with pattern ≤ 12 and flag $= 0$ have been used to ensure a high rejection of potentially distorting events such as can be caused by hot or flickering pixels or columns or features close to the CCD edges, especially at the readout nodes.

Inspection of the resulting light curves showed no obvious flares in the pn data (Fig. 2). MOS count rates were higher by up to a factor of ~4 in the beginning of the MOS observations compared to the remaining times (Fig. 3). MOS exposures started earlier than those for the pn camera; the lack of

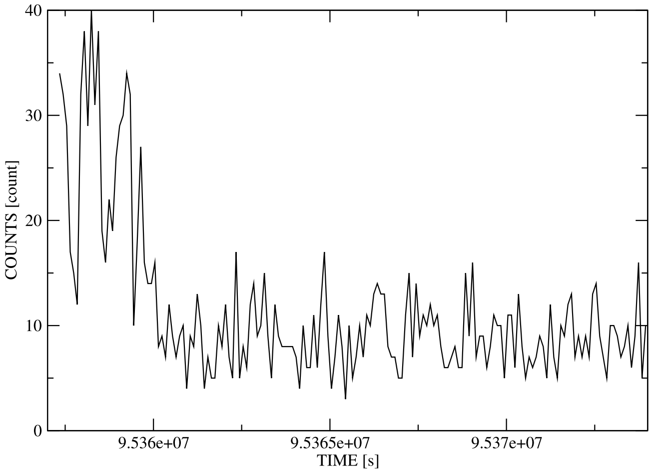

Fig. 3.—Light curve for MOS1 with 100 s binning.

---

[1] The *XMM-Newton* SAS Web site is at http://xmm.vilspa.esa.es/sas.

[2] The NASA Goddard Space Flight Center software package HEAsoft is available at http://heasarc.gsfc.nasa.gov/docs/software/lheasoft/ HEAsoft.

obvious flares in the pn is consistent with the MOS light curves for the overlapping time interval. The obviously contaminated times in the MOS observations were removed by taking into account only events with arrival times $\geq$95,360,200 s (*XMM-Newton* time) for all further steps.

Before calculating mean count rates in order to test for background flares, conservative "generic" cuts have been applied on the count rates, C_X. For pn, only times with $2 \leq C_X \leq 45$ counts per 100 s have been used; for MOS, only times with $1 \leq C_X \leq 25$ counts per 100 s have been used. The lower threshold is especially important for pn data in order not to bias the calculation of the mean count rate by inclusion of counting-mode times, times during which transmission of information for individual events of one or more (most likely all four) quadrants to the ground station does not occur.

For the final cuts, upper *and* lower thresholds are required in order to treat statistical fluctuations in both directions symmetrically. Here we choose to define the good time intervals (GTIs) by including only times where the count rates lie within $\pm 2\ \sigma$ of the mean count rates. For the individual detectors, the count-rate limits for GTIs are found to be 8–25 (pn), 3–15 (MOS1), and 2–15 (MOS2) counts per 100 s. The effective exposure time (live time) after this procedure results in 11 ks for pn and 13 ks for MOS1 and MOS2.

2.2. *Vignetting Correction*

Depending on the nature of a detected event, one should take into account vignetting caused by the baffles, mirrors, reflection grating array (for the MOS cameras only), etc., in the analysis. For instance, the X-ray photons from the target source (A1644) and the cosmic X-ray background (CXB) are vignetted in the same way. The soft protons show a different vignetting characteristic (but hopefully we got rid of most of those in § 2.1) and the PIB is not vignetted at all if the spatial variation of the fluorescent lines caused by the camera material itself is not interpreted as a vignetting characteristic. The noise in the CCDs, most easily visible as low-energy events close to the CCD edges, is not vignetted either.

In general, however, it is not easy to determine the nature of an individual event. The combination of methods for flare rejection, vignetting correction, and background subtraction employed here aims at a proper treatment of all components for the spectral analysis. This strategy involves correcting *all* events for the vignetting expected for X-ray photons, regardless of their nature at this point.

The vignetting depends on detector position and energy. The vignetting correction has been accomplished with the SAS task *evigweight*, which adds a weight column to the events file. The value of the weight is determined for each event by taking into account the detector position and energy of the event. Weights are assigned relative to the on-axis effective area so the weights have values $\geq$1. To accumulate images and spectra, these weights are summed up and errors are propagated including the vignetting correction.

2.3. *Background Subtraction*

In general, proper background subtraction is vital for an accurate spectral analysis of extended sources. In our case, the cluster emission fills most of the fields of view of the detectors, so it is difficult to determine the background from our observations. Thus, we determine the background from so-called blank-sky observations. The blank-sky observations are mostly high Galactic latitude observations of regions with very few bright sources. Several such observations have been combined for the EPIC cameras, mostly for the Thin filter in (mostly) FF mode (Lumb et al. 2002) to achieve good statistics and reduce the effects of cosmic/sample variance. We have made sure that for the energy range and signal-to-noise ratio (S/N) in spectral fits here, the differences in charge transfer inefficiency (CTI) corrections between the pn FF and EFF mode are not significant. The blank-sky observations are available at the *XMM-Newton* calibration Web site.[3]

The background observations have been recast on the sky in order to match the source observations using the SAS task *attcalc*.[4] This allows the use of sky coordinates for regional selections and at the same time allows estimates of the background from the same detector regions as the source, which in turn ensures that the significant variation of the fluorescent line emission with detector position is properly taken into account. By treating the blank-sky backgrounds identically to the data, the effect of incorrectly applying a vignetting correction to the PIB (in the source *and* background observations) is removed.

The same flare-rejection method (§ 2.1) has been applied to the background observations. The count-rate limits for GTIs here are found to be 8–31 (pn) and 2–16 (MOS1 and MOS2) counts per 100 s.

The PIB shows variation of ~8% (1 σ), as well as a long-term decrease of ~20% between the beginning of *XMM-Newton* observations and 2001 January (Katayama et al. 2004). In order to account for these variations, total field-of-view count rates of source and background observations have been calculated using the same energy, pattern, and flag selection criteria as for the GTI determination (§ 2.1). The source-to-background count-rate ratios 0.99 ± 0.03 (MOS1), 0.92 ± 0.03 (MOS2), and 0.88 ± 0.02 (pn) have been found (1 σ errors), consistent with the expected variation. For the calculation of these PIB scaling factors, the events have not been corrected for vignetting.

As mentioned in § 2.1, cleaning of flares in the high-energy bands generally used does not necessarily imply that all flares have been removed. Actually, we did find some weak remnant flares in the blank-sky observations when plotting light curves (GTI screened as described in § 2.1) in broad energy bands (see also Lumb et al. 2002). We therefore tested the variation in (10–12 keV) source-to-background count-rate ratios when calculating GTIs in the energy bands 7–12 and 0.3–12 keV for MOS1 and MOS2. We found that the variation is less than the (1 σ) statistical uncertainty and conclude that the influence of remnant flares is negligible for calculation of background scaling factors here.

To check whether the limitation to high-energy bands for the calculation of background scaling factors affects the results significantly, we have calculated them also using the energy ranges 0.3–14 keV (pn) and 0.3–12 keV (MOS). In this case, of course, only the CCD parts shielded from X-ray photons (and soft protons) are usable. We found results consistent with the total field-of-view results for pn and MOS1, and a slightly larger value for MOS2 (1.00 ± 0.02). In order to exclude the possibility that an imperfect correlation between the normalization of the continuum and the fluorescence lines (dependent on detector position) for the PIB

---

[3] The *XMM-Newton* calibration Web site is at http://xmm.vilspa.esa.es/external/xmm_sw_cal/calib/epic_1files.shtml.

[4] See Andy Read's *XMM-Newton* EPIC background analysis scripts at http://www.sr.bham.ac.uk/xmm3.

caused this slightly larger than expected variation, we also used the energy range 2–7 keV to calculate the background scaling factors. The results were consistent with the broader energy range used previously.

In summary, following these tests the background scaling factors 0.96 (MOS) and 0.88 (pn) have been assigned to the observations. Most of the tests above yield results consistent with the expected statistical uncertainties. To account for the difference between MOS and pn scaling factors, a conservative 8% systematic error has been added to the full energy range of all background spectra. Note also that it is implicitly assumed here (and in most other works that follow similar procedures) that the spectrum of the PIB does not vary when its normalization changes. Currently there seems to be no strong evidence for significant spectral variability (e.g., Katayama et al. 2004) apart from the fluorescence lines.

The main drawback of this method is that in general one gets the background contribution from the CXB wrong. The PIB dominates the hard part of the total background, but the CXB is important for the lower energies. Ideally, one would estimate the difference in the CXB contribution to source and background observations from a region with negligible source emission in the source observation or another observation very close by (e.g., Markevitch & Vikhlinin 2001; Pratt et al. 2001; Majerowicz et al. 2002; Arnaud et al. 2002). This is not feasible in the case of A1644 since cluster emission fills the entire field of view, and the only other *XMM-Newton* observation within 5° to date is likewise filled entirely with the emission of NGC 5044. Here we model a possible CXB difference in the spectral fitting procedure.

In order to estimate the spectral shape of a possible CXB difference between the source and background spectra, we have extracted spectra from an irregular region with decreased cluster emission in the northwestern part of the observation and fitted a two-temperature model. The model has a high-temperature component, which is supposed to account for the cluster emission, and a low-temperature, zero-redshift, solar-abundance component, which should represent the CXB excess relative to the background observations. The model fits indicate that in this region the cluster emission still dominates. The ratio of the number of cluster photons to CXB photons equals ~4 in the energy range 0.3–10 keV and ~2 in the energy range 0.3–0.5 keV. A best-fit value ∼0.2 keV is found for the low-temperature component. This estimate is consistent with values from studies of soft excess emission in other clusters (e.g., Kaastra et al. 2003). The origin of this component is uncertain; Kaastra et al. (2003) argue that it is due to intergalactic gas located around clusters. Our aim here is not to try to discuss the source of this soft CXB excess, but rather to determine its contribution to the cluster emission and account for it in the model fits (§ 2.4).

2.4. *Spectral Fitting*

Spectra from MOS1, MOS2, and pn have been fitted simultaneously. The same pattern and flag selections have been applied as for the generation of GTIs, except that only single and double events have been used for the pn camera. The response matrices were *m11_r7_im_all_2000-11-09.rmf*, *m21_r7_im_all_2000-11-09.rmf*, and *epn_ef20_sdY9.rmf* for MOS1, MOS2, and pn, respectively, in addition to on-axis ancillary response files created with the SAS task *arfgen*.

A comparison of individual pn single- and double-event spectral fits gives consistent results. The response of the pn camera depends on detector position. However, it has been verified that for the accuracy needed here use of the *epn_ef20_sdY0.rmf* response matrix does not result in significant changes of best-fit parameter values. Individual fit results from the three cameras are consistent with each other. Point sources and hot pixels have been excluded.

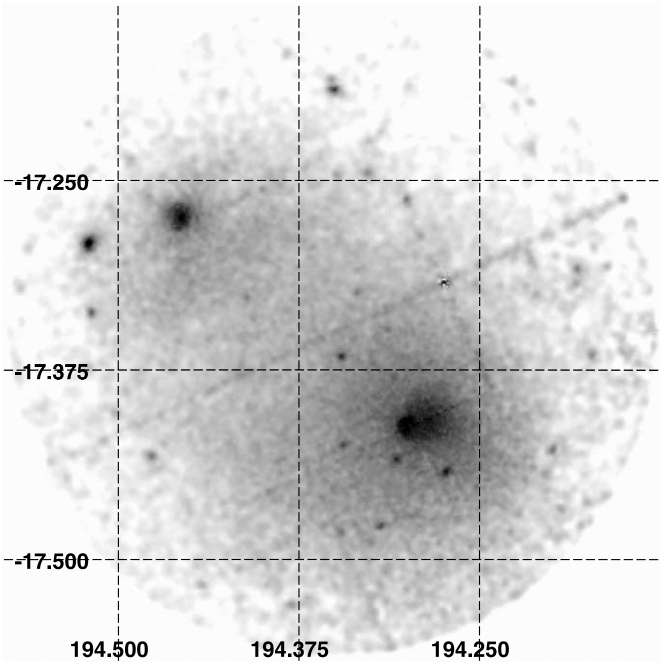

Fig. 4.—Background-, exposure-, and vignetting-corrected, adaptively smoothed combined MOS1-MOS2-pn count-rate image of A1644 in the energy range 0.3–5.0 keV (R.A. and decl. in equatorial coordinates, epoch J2000.0). The linear artifacts are due to an imperfect exposure correction near the chip boundaries.

XMM-Newton's point-spread function (PSF) is much improved compared to the PSFs of previous satellites capable of spatially resolved spectroscopy, e.g., *ASCA*. Nevertheless, for objects with strong temperature and surface brightness gradients its effect can become important. However, the main emphasis in this work is on the comparison of different segments of spectra at the same radii from cluster centers. In this case, radial PSF effects should not cause any artificial differences.

Spectral fits have been performed within XSPEC using a model $(wabs{*}\mathrm{MEKAL}) + \mathrm{MEKAL}$. Parameters for the second thermal component have been fixed at a redshift of zero, a metal abundance of $A = 1$ solar (Anders & Grevesse 1989), and a temperature of $kT_{\mathrm{X}} = 0.2$ keV, as discussed in § 2.3. The normalization is determined from the fits.

Source spectra have been regrouped to have at least 50 counts per bin. Spectral fits have been performed nominally in the energy range 0.3–10.0 keV for MOS and 0.3–12.0 keV for pn. All errors are quoted at the 90% confidence level for one interesting parameter unless noted otherwise.

3. RESULTS

3.1. *Imaging*

Figure 4 shows the combined MOS1-MOS2-pn image of nearly the full *XMM-Newton* field of view of A1644. The cluster has a very complicated surface brightness distribution on all scales. A main cluster to the southwest and a smaller subcluster to the northeast are easily identified. The emission surrounding both core regions is highly nonspherical. There is

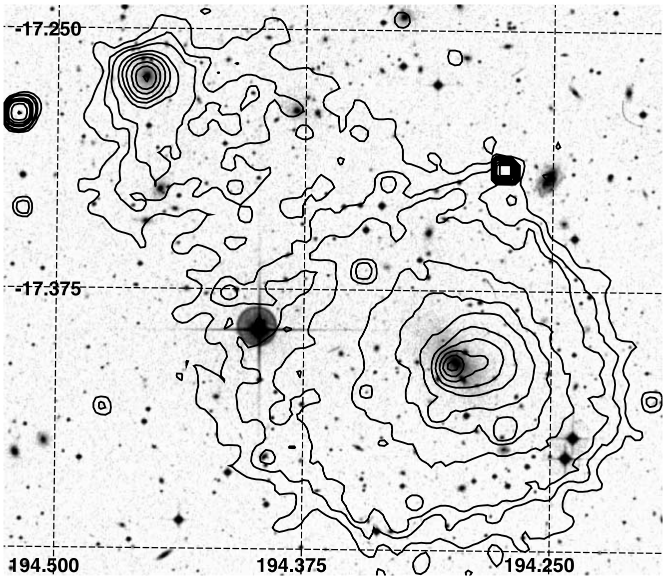

Fig. 5.—X-ray contours from the image in Fig. 4 overlaid onto an optical DSS image.

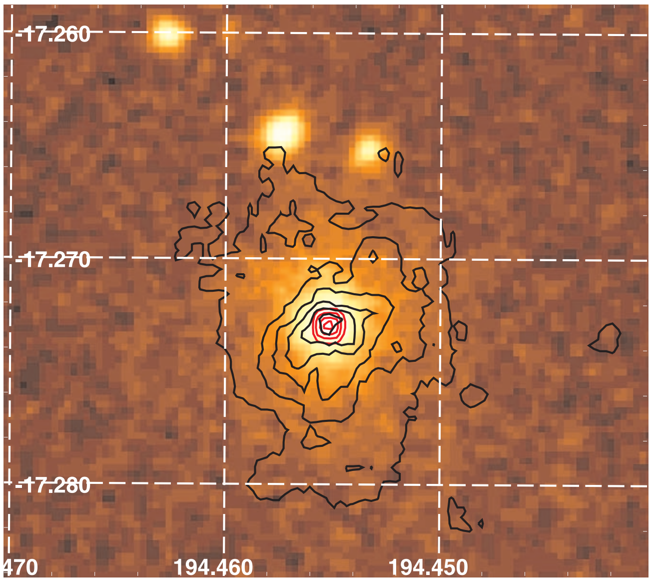

Fig. 7.—Same as Fig. 6, but for the subclump.

stronger emission to the south of the subclump than to the north. The core region of the main clump itself contains a displaced core-within-a-core.

The Digitized Sky Survey (DSS) image in Figure 5 shows that the X-ray peaks of the main cluster and subcluster coincide with two bright cluster galaxies (BCGs). The relative line-of-sight velocity component of the two central galaxies is ~600 km s^{-1}. The X-ray contours to the north of the subclump appear to be slightly compressed. Radio observations of the two BCGs show that they are both radio sources (e.g., Owen & Ledlow 1997).

The regions around the two BCGs are shown in more detail in Figures 6 and 7. Included are X-ray contours of a 19 ks *Chandra* observation taken on the same day as the *XMM-Newton* observation and available from the public archive. These contours illustrate the complexity of the emission in the cluster cores. Note that also in the very center of the subclump the X-ray contours to the north appear slightly compressed (Fig. 7). This apparent compression is on a much smaller scale than the compression already noted in Figure 5. Optical, radio, and X-ray centers coincide almost exactly for both subclusters.

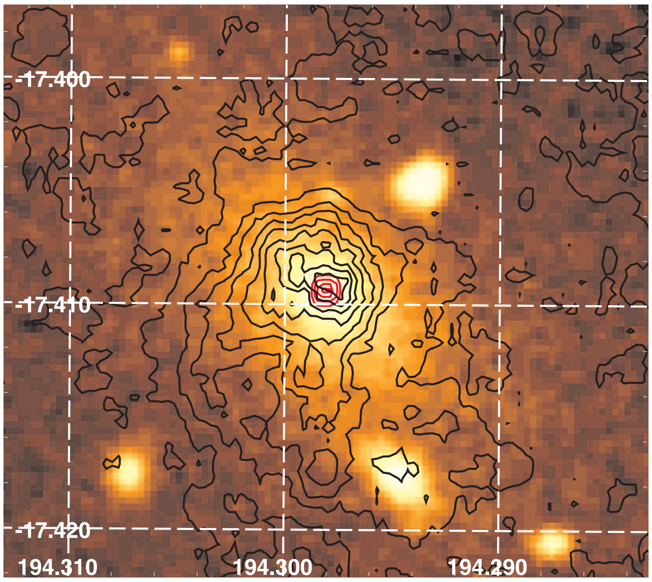

Fig. 6.—DSS image of the inner region of the main clump, overlaid with the X-ray contours from *Chandra* (*black*) and, in the very center, the 1.4 GHz radio data (*red*; from M. Ledlow, 2002, private communication).

3.2. *Spectroscopy*

The intracluster gas temperature is a fundamental observable for a gravitational cluster mass determination based on the hydrostatic assumption. The overall best-fit temperature based on a large elliptical region centered at R.A. = $194\overset{\circ}{.}356$, decl. = $-17\overset{\circ}{.}363$ encompassing both subclusters (semimajor axis = $733''$, semiminor axis = $528''$, position angle = 45°) is $kT_X = 3.83 \pm 0.06$ keV. The best-fit metal abundance is $0.32^{+0.02}_{-0.03}$ solar for the same region.

Note that the column density of neutral Galactic hydrogen, N_H, has been fixed at the value inferred from 21 cm radio measurements for our Galaxy (5.33×10^{20} cm^{-2}; Dickey & Lockman 1990[5]) for all results. In general, this value is marginally larger but consistent with best-fit values from direct spectral fits. Best-fit values for temperatures and abundances change only well within their uncertainties if the column density is treated as a free parameter.[6]

Figures 8 and 9 show the radial temperature profiles for the main clump and the subclump, respectively. Note that the center for the innermost bin of the main clump is offset from the center of the other bins in order to account for the core-within-a-core structure. The reduced χ^2 values (and the best-fit N_H values if left as a free parameter) for the innermost bin of both subclusters are too large (Tables 1 and 2). This is likely caused by higher temperature gas in the line of sight. For these two regions we therefore included a third thermal

---

[5] A FITS image from Dickey & Lockman (1990) is available at http://imagelib.ncsa.uiuc.edu/project/document/95.FL.01.

[6] Note that neglecting the CXB difference between source and background observations, i.e., fitting a model *wabs**MEKAL to the spectra here, results in N_H values significantly lower than the Galactic value or, if N_H is fixed to the Galactic value, to artificially decreased temperatures and increased χ^2.

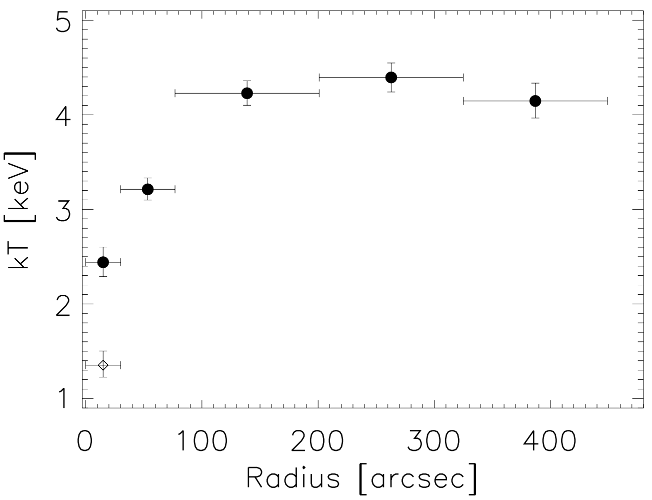

FIG. 8.—Radial temperature profile for the main clump. The open diamond shows the best-fit temperature if a third thermal component is included (see text).

component, i.e., the model $[wabs^{*}(\mathrm{MEKAL}+\mathrm{MEKAL})]+\mathrm{MEKAL}$ was fitted. The limited statistics require freezing the temperatures and abundances of the third components to the values found farther out. We therefore fixed the abundances at 0.5 solar and the temperatures at 3.5 and 3 keV for the main clump and the subclump, respectively. As a result, the best-fit central temperatures decrease further for both the main clump and the subclump (*open diamonds*).

Each of the two temperature profiles appears surprisingly similar to temperature profiles of relaxed, apparently undisturbed clusters: a drop in the center to about 1/3 of the ambient gas temperature, an isothermal structure in the outer parts, and weak indications for a slight temperature drop in the very outermost regions accessible.

TABLE 1

FIT RESULTS FOR THE MAIN CLUSTER PROFILE

Radial Range (arcsec)	kT_X (keV)	A	Reduced χ^2	Degrees of Freedom
0–30	$2.44^{+0.16}_{-0.15}$	$0.85^{+0.20}_{-0.16}$	1.80	103
0–30[a]	$1.35^{+0.15}_{-0.13}$	$0.94^{+1.11}_{-0.36}$	1.46	103
30–77	$3.21^{+0.12}_{-0.11}$	$0.73^{+0.09}_{-0.09}$	1.19	312
77–201	$4.23^{+0.13}_{-0.13}$	$0.33^{+0.05}_{-0.05}$	1.11	769
201–325	$4.39^{+0.15}_{-0.15}$	$0.24^{+0.05}_{-0.05}$	1.09	808
325–449	$4.15^{+0.19}_{-0.18}$	$0.21^{+0.06}_{-0.06}$	0.97	872

[a] Third thermal component applied (see text).

Note that the addition of a third component is only a crude approximation to account for effects caused by projection, PSF (see, e.g., Markevitch 2002; Majerowicz et al. 2002), and a possible real multiphase temperature structure. The reduced χ^2 values of the central bins become significantly smaller, but are still large even after addition of the third component. Also, these effects need not be limited to the central bins alone. A1644 is an extremely irregular object (see Figs. 4 and 12). This fact makes A1644 interesting but at the same time complicates deprojection attempts, for which spherical symmetry is usually assumed. In this work, we therefore focus on projected temperature estimates and qualitative comparisons to temperature maps of simulated clusters.

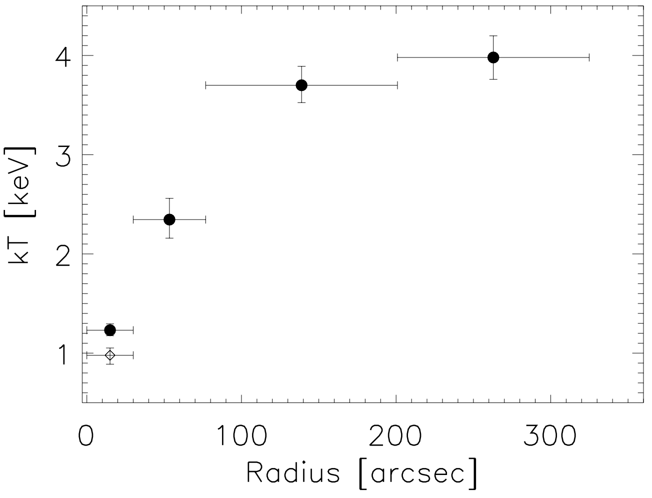

FIG. 9.—Same as Fig. 8, but for the subclump.

The corresponding metal abundance profiles are shown in Figures 10 and 11. In general, the abundances increase toward the centers of the two clumps, although there seems to be a drop in abundance in the innermost region of the subclump. However, this abundance drop vanishes when performing the fit with three thermal components (*open diamond*). This drop can therefore be regarded as artificial, even though it should be noted that the precise values depend on the temperature and abundance values adopted for the third component.

It is worth noting that weak indications for higher normalizations of the CXB excess emission toward the center of the main clump are found which may support the findings of Kaastra et al. (2003), although a discussion of the nature of the CXB excess is beyond the scope of this paper (see § 2.3).

Figure 12 shows a hardness ratio (HR) map. To create this map, source photon images from MOS1, MOS2, and pn (using only single events) in the energy band 2.0–10.0 keV have first been created and combined. Then the corresponding exposure maps have been created and combined, which also account for vignetting. Using the combined image and exposure map, an adaptively smoothed and exposure- and vignetting-corrected source image has been created with the SAS task *asmooth* ($\mathrm{S/N}=15$). Subsequently, a similarly created (though simply smoothed with $\sigma=7.5$), exposure- and vignetting-corrected combined background image has been subtracted from the source image. The same procedure has been followed to create an image in the 0.3–2.0 keV energy band, using the same smoothing templates as created for the 2.0–10.0 keV image. The ratio of the latter two images is shown in Figure 12. Soft emission is shown in dark and hard emission in bright. We have verified that using the source smoothing template also for smoothing the background

TABLE 2

FIT RESULTS FOR THE SUBCLUSTER PROFILE

Radial Range (arcsec)	kT_X (keV)	A	Reduced χ^2	Degrees of Freedom
0–30	$1.23^{+0.06}_{-0.06}$	$0.28^{+0.07}_{-0.05}$	2.65	54
0–30[a]	$0.98^{+0.07}_{-0.09}$	$0.55^{+0.50}_{-0.29}$	1.75	54
30–77	$2.35^{+0.21}_{-0.19}$	$0.44^{+0.14}_{-0.12}$	1.27	108
77–201	$3.70^{+0.19}_{-0.17}$	$0.49^{+0.10}_{-0.09}$	0.96	404
201–325	$3.98^{+0.22}_{-0.22}$	$0.29^{+0.08}_{-0.08}$	0.89	570

[a] Third thermal component applied (see text).

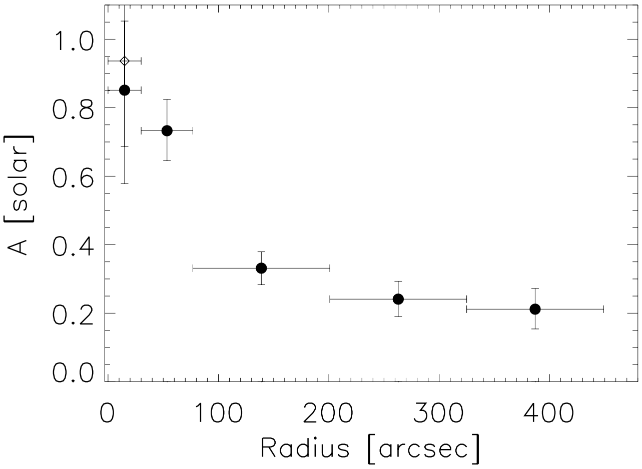

FIG. 10.—Metal abundance profile for the main clump. The open diamond shows the best-fit abundance if a third thermal component is included.

image does not result in significant changes in the relevant region. Note that the CXB excess emission has not been subtracted in the HR map. This may bias the HR map in the outermost regions of the observation. However, we find below that spectral fits that take the CXB excess into account correspond well to the features seen in the HR map. Therefore, it is not expected that the region shown is biased significantly.

In Figure 13, an adaptively binned temperature map is shown. The map has been created using all three detectors and making use of the Interactive Spectral Interpretation System (ISIS; Houck & Denicola 2000). The pixel size is 14.″4. Pixels are nearly independent at the center of the main clump, but are correlated in other regions. The actual spectral extraction region used for the fits depends on the surface brightness; the largest extraction region is 1′ on a side. Most pixels shown black had fewer than 800 source counts using the maximum smoothing scale. A few more pixels with a negative error of more than 30% were masked out. The abundance of the main MEKAL component has been fixed here at the average value 0.32 solar (§ 3.2). The features seen in the HR map (discussed in detail below) seem to correspond to features in the temperature map. This indicates the consistency of both approaches and we use the HR map, which is more closely related to the data, as guidance below.

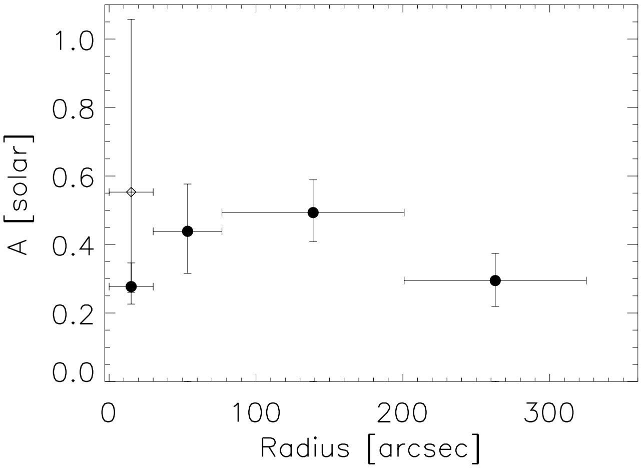

FIG. 11.—Same as Fig. 10, but for the subclump.

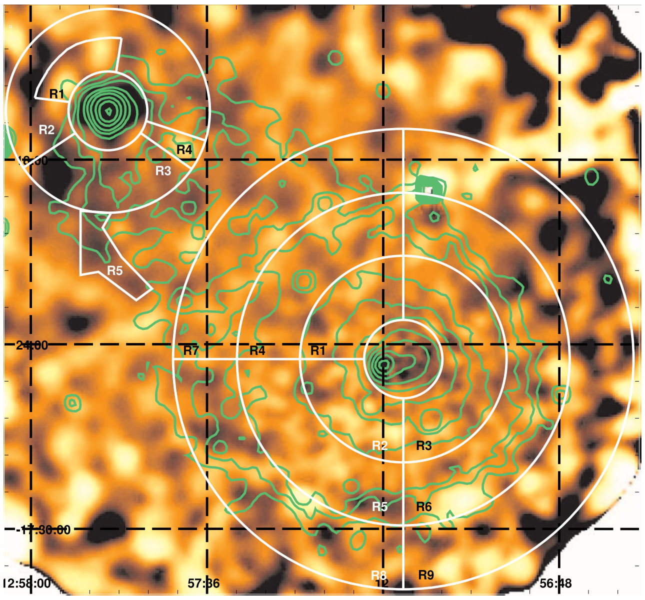

FIG. 12.—HR map of A1644, based on the ratio of the combined MOS1-MOS2-pn count rates in the energy bands 0.3–2.0 keV and 2.0–10.0 keV. The map has been corrected for background, exposure, and vignetting and is adaptively smoothed. Soft emission appears dark and hard emission bright. Also shown are surface brightness contours from Fig. 5 and regions selected for spectral analysis.

The HR map and the X-ray image suggest a number of interesting regions in the cluster that may have differing temperatures and/or abundances. In general, clusters as irregular as A1644 often show more complex temperature structure. Therefore, we also extracted spectra in segments of annuli for the main clump. The radial boundaries for the nine segments of the main cluster correspond to the ranges for the three outermost annuli given in Table 1. Figure 12 shows these and other selected regions as well as surface brightness contours overlaid onto the HR map. (Note that the cluster emission extends beyond the outermost shown surface brightness contour.)

Best-fit temperature and metal abundance values for the segments are shown in Figures 14 and 15 (and Table 3),

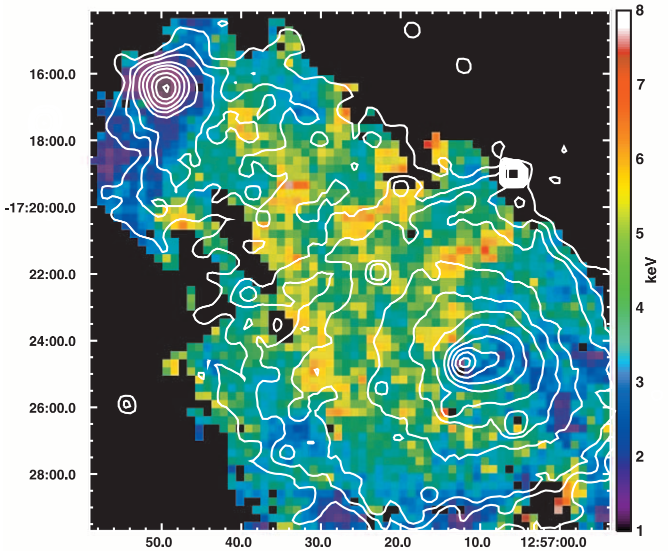

FIG. 13.—Temperature map of A1644. Also shown are surface brightness contours from Fig. 5.

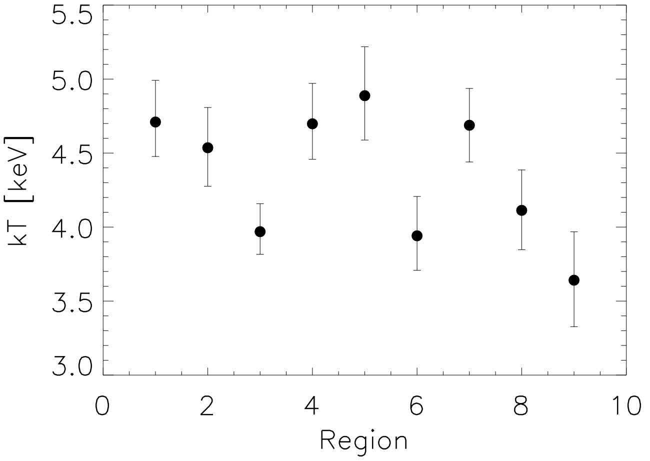

FIG. 14.—Gas temperature determinations of selected regions of the main clump (see Fig. 12).

respectively. It is apparent that there is significant nonradial temperature structure, and that the relatively regular radial temperature profile in Figure 8 is the result of averaging over annuli with large azimuthal temperature variations. In particular, the temperatures of the segments to the west of the main clump (R3, R6, and R9) are all significantly lower than all regions to the east (R1, R2, R4, R5, and R7) except for R8. These findings correspond well to those in the HR map (Fig. 12).

We also determined temperatures and abundances for more complicated regions selected as being of interest based on the *XMM-Newton* image and the HR map. This allows us to search for cool/metal-rich trails (dark in the HR map) or hot spots (bright in the HR map). Whether brightness fluctuations in the HR map correspond to significant temperature/abundance changes is evaluated by direct spectral fits of selected regions. Note that not all artifacts, e.g., inexact exposure correction close to CCD chip boundaries, have been removed in the HR map in Figure 12. The spectral analysis, however, is not affected by this.

TABLE 3

FIT RESULTS FOR THE MAIN CLUSTER REGIONS

Region	kT_X (keV)	A	Reduced χ^2	Degrees of Freedom
1.........................	$4.71^{+0.28}_{-0.23}$	$0.32^{+0.10}_{-0.10}$	1.06	259
2.........................	$4.54^{+0.27}_{-0.26}$	$0.33^{+0.10}_{-0.10}$	1.08	267
3.........................	$3.97^{+0.19}_{-0.15}$	$0.41^{+0.08}_{-0.07}$	0.96	439
4.........................	$4.70^{+0.27}_{-0.24}$	$0.22^{+0.09}_{-0.08}$	1.07	289
5.........................	$4.89^{+0.33}_{-0.30}$	$0.17^{+0.09}_{-0.09}$	0.94	316
6.........................	$3.94^{+0.27}_{-0.23}$	$0.27^{+0.10}_{-0.09}$	1.11	410
7.........................	$4.69^{+0.25}_{-0.25}$	$0.22^{+0.08}_{-0.08}$	0.83	318
8.........................	$4.11^{+0.27}_{-0.27}$	$0.24^{+0.10}_{-0.10}$	1.03	340
9.........................	$3.64^{+0.33}_{-0.31}$	$0.18^{+0.11}_{-0.11}$	0.93	413

The region to the south of the subclump (R3) appears fairly soft, whereas a small region to the southeast (R4) appears hard. The spectral fit results (Fig. 16 and Table 4) reveal that the temperature determination for R3 is indeed significantly lower than the value for the rest of this annulus (R2, which excludes R1) and especially than that for R4. Furthermore, the metal abundance of R3 appears enhanced (Fig. 17). The best-fit temperature for R5 (the small dark tail to the south of R3 in Fig. 12) is similar to that for R3. On the other hand, R1, the region north-northeast of the subclump, has a high temperature similar to R4.

4. DISCUSSION

We first consider some implications of these observations for the use of clusters of galaxies as cosmological probes. How much do the X-ray flux estimates based on resolved observations differ from simple estimates based on global measurements, such as those for clusters only observed with the *ROSAT* All-Sky Survey (RASS)? How much do mass estimates differ when only a broad-beam overall gas temperature estimate is available?

The overall flux from A1644, which extends beyond *XMM-Newton*'s field of view, is $f_X(0.1-2.4\text{ keV}) = 4.03 \times 10^{-11}$ ergs s^{-1} cm^{-2} (Reiprich & Böhringer 2002) based on RASS data. (A1644 was not observed in pointed mode with *ROSAT* PSPC.) It is worth noting that A1644 has been treated as a single cluster in the HIFLUGCS (Reiprich & Böhringer 2002) and REFLEX (Böhringer et al. 2001) catalogs, primarily because of the limited exposure time (<300 s) of the RASS at A1644's position and the relatively small projected separation of the two cluster components. The *XMM-Newton*

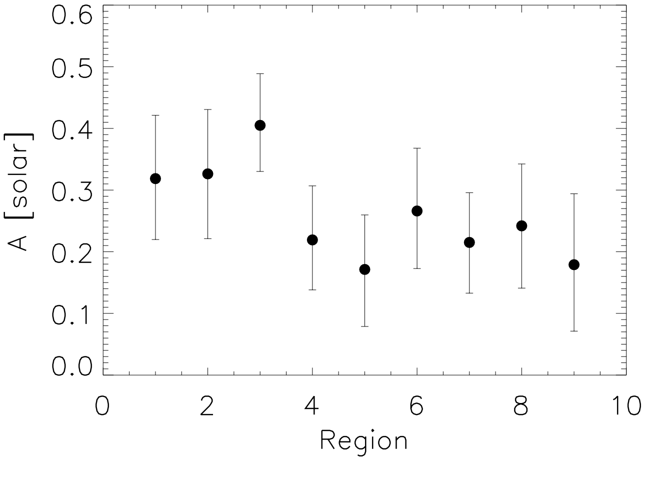

FIG. 15.—Metal abundance determinations of selected regions of the main clump.

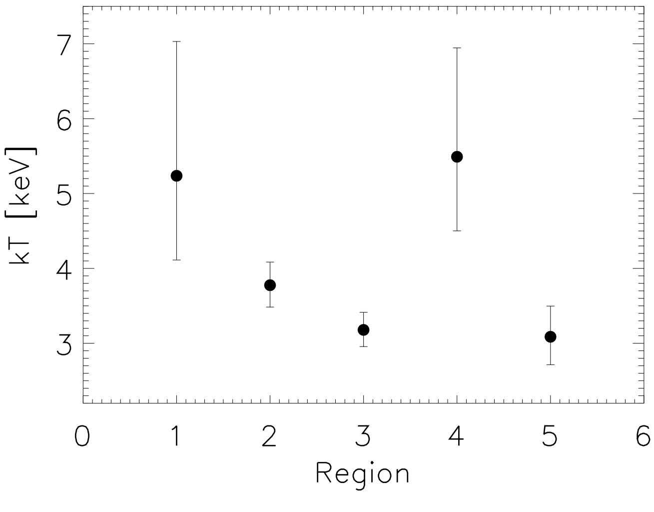

FIG. 16.—Gas temperature determinations of selected regions of the subclump.

TABLE 4

Fit Results for the Subcluster Regions

Region	kT_X (keV)	A	Reduced χ^2	Degrees of Freedom
1	$5.24^{+1.79}_{-1.12}$	$0.70^{+1.34}_{-0.70}$	0.89	30
2	$3.78^{+0.31}_{-0.29}$	$0.36^{+0.13}_{-0.13}$	0.92	217
3	$3.18^{+0.24}_{-0.22}$	$0.59^{+0.14}_{-0.13}$	1.27	165
4	$5.49^{+1.45}_{-0.99}$	$0.42^{+0.69}_{-0.42}$	1.46	31
5	$3.09^{+0.41}_{-0.37}$	$0.31^{+0.24}_{-0.22}$	1.28	45

image indicates that the X-ray flux (f_X) ratio between the main clump and the subclump is ~3:1. This means that instead of one cluster with $f_X \approx 4 \times 10^{-11}$ ergs s^{-1} cm^{-2}, one actually has two clusters with about $f_X \approx (3 \text{ and } 1) \times 10^{-11}$ ergs s^{-1} cm^{-2} each. This could affect luminosity and mass functions significantly if such major mergers were common. The effect of an incorrect treatment would be to artificially increase the number of high-mass clusters and decrease the number of low-mass clusters. Using the shape of the mass function to constrain the cosmic mass density, Ω_m, and the amplitude of mass fluctuations, expressed as σ_8, individually would then result in artificially low values for Ω_m and high values for σ_8. With the ongoing analysis of the complete sample of HIFLUGCS clusters with *Chandra* and *XMM-Newton*, we will be able to quantify the fraction of such clusters and their influence on derived cosmological parameters, as well as study the difficulty of estimating survey selection functions in the vicinity of bright clusters (due not only to double clusters but also line-of-sight projections) in general.

A simple broad-beam temperature estimate may be biased low compared to the ambient gas temperature because of cool emission in the dense (high-emissivity) cores. For instance, the temperature in a large annulus around the main clump in A1644 (201″–325″) is 4.40 keV. If we take this as the ambient temperature that is characteristic of the cluster gravitational potential, it is a factor of 1.15 higher than a broad-beam temperature estimate including both clumps (3.83 keV). Since $M \propto T^{1.5} - T^{2.0}$ (e.g., Finoguenov et al. 2001), this factor translates into an underestimate of a factor of 1.23–1.32 in the cluster mass.

The surface brightness structure of both subclumps is obviously messy. However, the radial temperature profiles (Figs. 8 and 9) are smooth and appear rather similar to profiles of relaxed clusters (e.g., compare to Fig. 1 in Allen et al. 2001). This might suggest that A1644 is moderately relaxed, and that the temperature structure may not be strongly affected by the interaction of the two subclumps. However, a more detailed examination of the thermal structure shows that the cluster is not at all relaxed. As the HR map (Fig. 12) indicates and Figures 14 and 16 confirm, the temperature structure is also quite complex. The region between the two clumps is significantly hotter than the region to the west of the main clump (the region that appears least disturbed in X-ray surface brightness). This may indicate that the gas in the region between the clumps has been heated up by adiabatic compression or shocks. Also, the core-within-a-core structure of the main clump (Fig. 4) may be caused by core oscillations induced by the passage of the subclump (e.g., Tittley & Henriksen 2003) or possibly by a remnant of a previous merger.

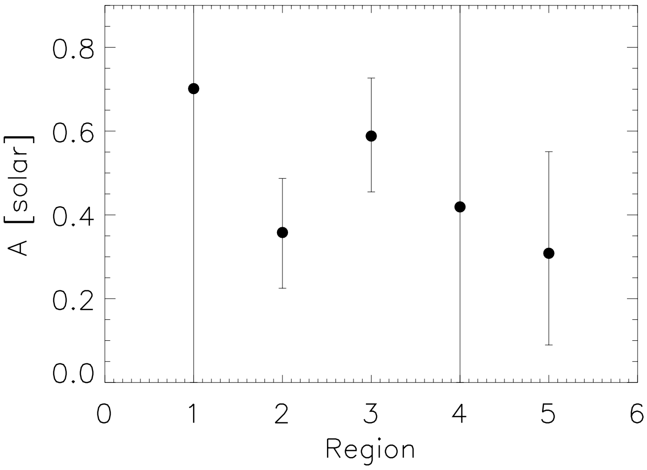

Fig. 17.—Metal abundance determinations of selected regions of the subclump.

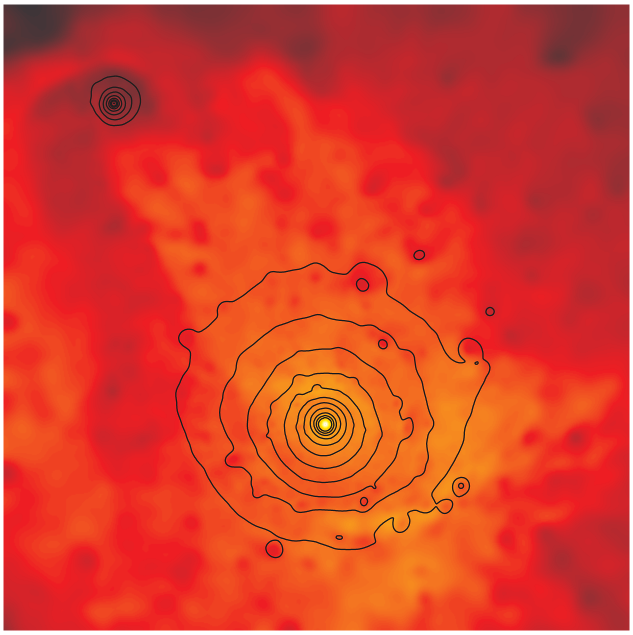

Fig. 18.—Mass-weighted temperature map from a hydrodynamic simulation. Temperature increases from black to red to yellow. Also shown are X-ray surface brightness contours.

Furthermore, both the surface brightness and temperature structure around the subclump are peculiar. Based on the X-ray image, the gas appears to be slightly compressed to the north and clearly elongated to the south and west. This suggests that this subclump is moving through the ICM of the main clump and losing some fraction of its gas in a trail behind the core of the subclump. Given this dynamical picture, what temperature structure might be expected? One may expect heated gas in front of the subclump (projected roughly to the north) because of adiabatic compression or shocks. One might also expect the trail to the south to consist of somewhat cooler, more metal-rich gas stripped from the subclump. This appears to be consistent both with the HR map and with the extracted spectra in the subclump regions R1, R3, and R5.

Figures 5 and 7 show that the X-ray peak of the subclump and the optical center of the brightest galaxy coincide. This suggests that the subclump has not passed through the core of the main clump; if it had, the very high ram pressure would have stripped the subclump core, which would lag behind the collisionless dark matter and galaxies (e.g., Markevitch et al.

2002). The angle of the cool, metal-rich gas trail also suggests an off-center collision. One concern with this picture is that the dense gas in the core of the subclump would then be interacting with lower density gas in the outer parts of the main clump. Would one expect the dense subcluster to lose an observable amount of gas during its travel through the ICM?

We have compared A1644 to a hydrodynamic simulation of a small cluster undergoing an off-axis merger with a larger cluster. This simulation was done completely independently; no effort was made to adjust the initial conditions to match the observation of A1644. The temperature map of this simulation at a time when the smaller cluster has passed by the core of the main cluster for the first time is shown in Figure 18. Comparison to the HR map of A1644 (Fig. 12) shows an interesting similarity. There is hotter gas in front of the smaller cluster and cooler, ram-pressure–stripped gas behind. This trail of stripped gas cools adiabatically as it expands. There is a hotter region to the southwest, which is similar to region R4 seen in A1644. The larger scale $T_{\rm X}$ distribution around the main cluster in the simulation is also similar to that observed in A1644. There appears to be slightly cooler gas to the southeast in the simulation due to stripped gas from the smaller cluster, which agrees with the R8 region in the HR map and spectra.[7]

The indication of an increased metal abundance in the cool trail of A1644's subclump makes other scenarios such as cooling of intracluster gas onto the moving subclump (as seen in A1795 on much smaller scales; Fabian et al. 2001) more difficult to reconcile with the data. Note that the radio source in the center of the subclump (Fig. 7) may provide additional energy for gas removal from central denser regions.

5. SUMMARY

XMM-Newton imaging spectroscopy of the galaxy cluster A1644 has shown two subclusters undergoing an off-axis merger with remarkable detail. The X-ray analysis is also supported by optical data on the cluster, and the resulting dynamical picture agrees very well with an independent hydrodynamic simulation of such an off-axis merger. The findings imply that we see gas that has been removed from the smaller subcluster, possibly by ram pressure from the motion through intracluster gas of the main clump, possibly augmented by the effect of the central radio source of this subclump.

The code used to create the X-ray temperature map made use of the Interactive Spectral Interpretation System (ISIS; Houck & Denicola 2000). M. Ledlow (2002, private communication) made available the radio images. This work was supported by NASA *XMM-Newton* grants NAG5-10075, NAG5-13088, and NAG5-13737. T. H. R. acknowledges support by the Celerity Foundation through a postdoctoral fellowship. The *XMM-Newton* project is an ESA Science Mission with instruments and contributions directly funded by ESA Member States and the USA (NASA). The Digitized Sky Surveys were produced at the Space Telescope Science Institute under US Government grant NAG W-2166. The images of these surveys are based on photographic data obtained using the Oschin Schmidt Telescope on Palomar Mountain and the UK Schmidt Telescope. This publication makes use of data products from the Two Micron All Sky Survey (2MASS), which is a joint project of the University of Massachusetts and IPAC/Caltech, funded by NASA and NSF.

---

[7] An animation of this simulation is available at http://A1644.dark-energy.net. Note that cool trails from subclusters are commonly seen in simulations. Compare, e.g., to the simulations by Motl et al. (2004); see also the Power Point presentation available at http://www.astro.virginia.edu/coolflow/abs.php?regID=184.

REFERENCES

Allen, S. W., Schmidt, R. W., & Fabian, A. C. 2001, MNRAS, 328, L37
Anders, E., & Grevesse, N. 1989, Geochim. Cosmochim. Acta, 53, 197
Arnaud, M., et al. 2002, A&A, 390, 27
Bahcall, N. A. 2000, Phys. Rep., 333, 233
Böhringer, H., et al. 2001, A&A, 369, 826
Dickey, J. M., & Lockman, F. J. 1990, ARA&A, 28, 215
Ettori, S., & Fabian, A. C. 2000, MNRAS, 317, L57
Fabian, A. C., Sanders, J. S., Ettori, S., Taylor, G. B., Allen, S. W., Crawford, C. S., Iwasawa, K., & Johnstone, R. M. 2001, MNRAS, 321, L33
Finoguenov, A., Reiprich, T. H., & Böhringer, H. 2001, A&A, 368, 749
Girardi, M., Escalera, E., Fadda, D., Giuricin, G., Mardirossian, F., & Mezzetti, M. 1997, ApJ, 482, 41
Houck, J. C., & Denicola, L. A. 2000, in ASP Conf. Ser. 216, Astronomical Data Analysis Software and Systems IX, ed. N. Manset, C. Veillet, & D. Crabtree (San Francisco: ASP), 591
Jones, C., & Forman, W. 1999, ApJ, 511, 65
Kaastra, J. S., Lieu, R., Tamura, T., Paerels, F. B. S., & den Herder, J. W. 2003, A&A, 397, 445
Katayama, H., Takahashi, I., Ikebe, Y., Matsushita, K., Tanaka, Y., & Freyberg, M. 2004, A&A, 414, 767
Kempner, J. C., Sarazin, C. L., & Ricker, P. M. 2002, ApJ, 579, 236
Lumb, D. H., Warwick, R. S., Page, M., & De Luca, A. 2002, A&A, 389, 93
Majerowicz, S., Neumann, D. M., & Reiprich, T. H. 2002, A&A, 394, 77
Markevitch, M. 2002, preprint (astro-ph/0205333)
Markevitch, M., Gonzalez, A. H., David, L., Vikhlinin, A., Murray, S., Forman, W., Jones, C., & Tucker, W. 2002, ApJ, 567, L27
Markevitch, M., Sarazin, C. L., & Vikhlinin, A. 1999, ApJ, 521, 526
Markevitch, M., & Vikhlinin, A. 2001, ApJ, 563, 95
Markevitch, M., et al. 2000, ApJ, 541, 542
———. 2003, ApJ, 586, L19
———. 2004, ApJ, in press
Motl, P. M., Burns, J. O., Loken, C., Norman, M. L., & Bryan, G. 2004, ApJ, in press (astro-ph/0302427)
Owen, F. N., & Ledlow, M. J. 1997, ApJS, 108, 41
Pratt, G. W., Arnaud, M., & Aghanim, N. 2001, in 21st Moriond Astrophysics Meeting, Galaxy Clusters and the High-Redshift Universe Observed in X-Rays, ed. D. M. Neumann & J. T. T. Van (Gif-sur-Yvette: Editiones Frontiers), http://www-dapnia.cea.fr/Conferences/Morion_astro_2001/abs03/pratt.html
Randall, S. W., Sarazin, C. L., & Ricker, P. M. 2002, ApJ, 577, 579
Reiprich, T. H., & Böhringer, H. 2002, ApJ, 567, 716
Ricker, P. M., & Sarazin, C. L. 2001, ApJ, 561, 621
Sarazin, C. L. 2002, in Merging Processes in Galaxy Clusters, ed. L. Feretti, I. M. Gioia, & G. Giovannini (Dordrecht: Kluwer), 1
Spergel, D. N., & Steinhardt, P. J. 2000, Phys. Rev. Lett., 84, 3760
Tittley, E. R., & Henriksen, M. 2003, AAS HEAD Meeting, 35, 13.06
Tustin, A. W., Geller, M. J., Kenyon, S. J., & Diaferio, A. 2001, AJ, 122, 1289
Vikhlinin, A., Markevitch, M., & Murray, S. S. 2001a, ApJ, 549, L47
———. 2001b, ApJ, 551, 160
White, D. A., Jones, C., & Forman, W. 1997, MNRAS, 292, 419
Zabludoff, A. I., Geller, M. J., Huchra, J. P., & Vogeley, M. S. 1993, AJ, 106, 1273